

Growth and physical properties of BiFeO₃ thin films directly on Si substrate

Xiaokang Yao^{a,b}, Can Wang^{a,b,c,*}, Shilu Tian^{a,b}, Yong Zhou^{a,b}, Xiaomei Li^{a,b}, Chen Ge^a, Er-jia Guo^{a,d}, Meng He^a, Xuedong Bai^{a,b}, Peng Gao^e, Guozhen Yang^{a,b}, Kuijuan Jin^{a,b,c,*}

^a Beijing National Laboratory for Condensed Matter Physics, Institute of Physics, Chinese Academy of Sciences, Beijing 100190, China

^b University of Chinese Academy of Sciences, Beijing 100049, China

^c Songshan Lake Materials Laboratory, Dongguan, Guangdong 523808, China

^d Center of Materials Science and Optoelectronics Engineering, University of Chinese Academy of Sciences, Beijing 100049, China

^e International Center for Quantum Materials and Electron Microscopy Laboratory, School of Physics, Peking University, Beijing 100871, China



ARTICLE INFO

Communicated by K.H. Ploog

Keywords:

A1. X-ray diffraction

A3. Thin film

A3. Laser-molecular beam epitaxy

B2. Multiferroic BiFeO₃

B2. Semiconductor Si

ABSTRACT

Multiferroic BiFeO₃ thin films have been widely studied for their intriguing fundamental physics and exotic functional properties. Integration of the BiFeO₃ thin films with semiconductor Si is crucial for the practical development of novel electronic and photosensitive devices. Here, we report the fabrication and physical properties of BiFeO₃ thin films grown directly on bare Si substrate by laser-molecular beam epitaxy. It was found that a predeposition process performed at room temperature and high vacuum conditions is effective and necessary for obtaining the pure-phase BiFeO₃ thin films. X-ray diffraction measurements indicate that the obtained BiFeO₃ thin films are in a single-phase polycrystalline state and show improved crystallinity with increasing thickness, and a transmission electronic microscopy image illustrates an interface layer around 3 nm in thickness existing between the BiFeO₃ thin films and Si substrate. Electrical measurements show that the BiFeO₃ thin films have good ferroelectricity and low leakage current. Moreover, optical properties investigated by spectroscopic ellipsometry demonstrate that the direct band gap of the thin films increases with decreasing thickness.

1. Introduction

Complex transition metal oxides have tantalizing functional properties due to the existence of spin, charge, orbital and lattice degrees of freedom and the coupling among them [1–3]. The growth of complex transition metal oxides on Si substrates has attracted much attention due to the requirements of integrating multifunctional materials with advanced semiconductor technology. Typically, researchers predicted, in early times, that ferroelectric oxide materials can be used to replace SiO₂ in metal-oxide-semiconductor field-effect transistors (MOSFET) in order to create innovative devices, such as ferroelectric FET. This can take advantage of the character of nonvolatile polarization of ferroelectrics, enabling transistor to still keep either on or off in the absence of applied electric fields [4]. Among these compound oxides systems, multiferroic BiFeO₃ (BFO) has the coupling of magnetic and electric orders, showing the single-phase magnetoelectric characteristics at room temperature [5,6]. It possesses a rhombohedrally distorted perovskite structure (space group R3c) with lattice constant $a = 5.634 \text{ \AA}$, $\alpha = 59.348^\circ$ and can be represented as pseudo-cubic structure with unit cell parameters $a = 3.965 \text{ \AA}$ and an inner angle of

89.46° [7–9]. As a rare multiferroic material at room temperature, BFO thin films have been the focus in the research fields of ferroelectric and multiferroic [10–15]. For the growth of BFO thin films on Si substrate, many kinds of oxides have been used as the buffer layer between BFO and Si substrates, in order to reduce the lattice mismatch and mutual diffusion [8,16–19]. Up to now, there are very few reports about BFO thin films grown directly on the bare silicon, and the reported BFO thin films almost have no detectable ferroelectricity [20,21].

In this work, BFO thin films having a single-phase polycrystalline structure with good ferroelectricity were grown directly on conducting silicon by using laser-molecular beam epitaxy (Laser-MBE). Ferroelectric hysteresis loops (P - E loops), I-V characteristics (expressed by leakage current density versus electric field curves) and optical properties of the BFO thin films with different thickness were investigated.

2. Experimental section

As-received p -type conducting Si substrates were cleaned separately about 10 min using alcohol, acetone, and deionized water in sequence,

* Corresponding authors at: Beijing National Laboratory for Condensed Matter Physics, Institute of Physics, Chinese Academy of Sciences, Beijing 100190, China.
E-mail addresses: canwang@iphy.ac.cn (C. Wang), kjjin@iphy.ac.cn (K. Jin).

<https://doi.org/10.1016/j.jcrysgr.2019.06.017>

Received 27 April 2019; Received in revised form 9 June 2019; Accepted 13 June 2019

Available online 14 June 2019

0022-0248/ © 2019 Elsevier B.V. All rights reserved.

and then dipped into buffered hydrofluoric acid solution for 40 s to remove the native oxide on the surface and to form a hydrogen-terminated surface. Then the Si substrate was transferred immediately into the Laser-MBE deposition chamber with a load lock. A focused pulsed 308 nm excimer laser beam was used to ablate the Bi-rich ceramic target ($\text{Bi}_{1.3}\text{FeO}_3$) with an energy density of about 1.5 J/cm^2 at a repetition rate of 4 Hz. Firstly, as a predeposition process, an initial BFO thin layer in about 2 nm thickness was deposited on the Si surface at room temperature in the base pressure of around 5×10^{-6} Pa. The aim of the predeposition was to reduce the formation of the amorphous SiO_2 layer at the Si surface. After the predeposition, the substrate was heated up to 600°C and then flowing oxygen was introduced into the chamber and kept at around 10 Pa. BFO was continuously deposited on the initial BFO thin layer to the final anticipated thickness. All the thin films were annealed *in situ* for 10 min and then cooled down to room temperature at a rate of 10°C/min .

X-ray diffraction (XRD, Ultima VI) measurements were carried out to analyze phase structure of thin films. Atomic force microscope (AFM, Asylum Research Ryan's MFP-3D™) was used to characterize the surface topography and measure grain size of the thin films with different thickness. Transmission electron microscopy (TEM, JEOL2010F) was employed to characterize the cross-sectional image of the BFO/Si interface. High-angle annular dark field scanning TEM (HAADF-STEM) and energy-dispersive spectroscopy (EDS) were used to analyze the structure and chemical constituent of the BFO/Si interface. Piezoelectric force microscope (PFM) and ferroelectric tester (Radiant ferroelectric tester Premier II) were used to measure the ferroelectric domain states and the polarization hysteresis loops. Keithley 2400 Source Meter was employed to measure current density versus electric field curves, and the photocurrent density was taken via vertical irradiation on the surface of BFO thin films using a 375 nm excimer laser. Optical properties of BFO thin films were investigated by spectroscopic ellipsometry (RC2-D).

3. Results and discussion

Fig. 1 shows the θ - 2θ X-ray diffraction patterns for the BFO thin films. The bottom black curve is for the BFO thin film grown without the predeposition process, and the color curves are for the BFO thin films grown with the predeposition process in thickness of 110 nm

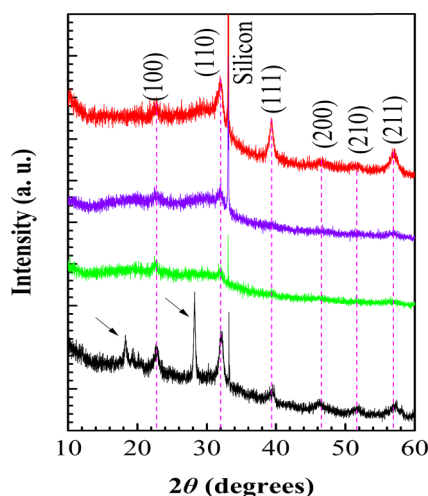


Fig. 1. X-ray diffraction (XRD) patterns of the BFO thin films on *p*-type Si (1 0 0) substrates. The film showing impurity phase (indicated by arrows in the black curve) was grown without the predeposition and the others with different thickness (110 nm in green, 270 nm in violet, and 460 nm in red) were grown with a predeposition. The pseudo-cubic notation is used for the BFO thin films. (For interpretation of the references to colour in this figure legend, the reader is referred to the web version of this article.)

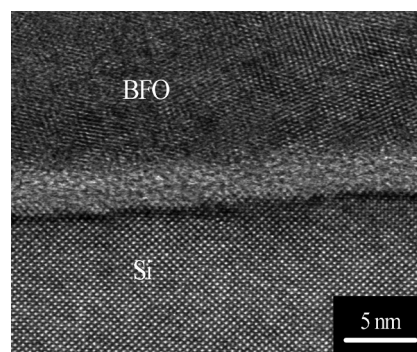


Fig. 2. Cross-sectional TEM image of the BFO/Si interface. There is an amorphous interfacial layer around 3 nm in thickness between the BFO thin film and Si substrate.

(green), 270 nm (violet), and 460 nm (red), respectively. It can be seen that the film grown without the predeposition shows diffraction peaks from impurity phases marked by arrows, while the thin films grown with the predeposition show a single-phase polycrystalline structure and don't have any impurity phases. It indicates that the predeposition process is effective and necessary to avoid the formation of impurity phase. The intensity of the diffraction peaks increases obviously with film thickness, which may suggest a good crystallinity for the thicker films. In general, an interface layer between oxide thin film and Si substrate can be formed inevitably during the oxide film growth [22]. To reveal the interface between the BFO thin film and Si substrate, a cross-sectional transmission electron microscopy image has been taken from the interface of the BFO/Si, as shown in Fig. 2. The observed amorphous interface layer is only around 3 nm in thickness, which means the predeposition layer may have effectively prevented the further increase of the interface layer at high temperature and oxygen ambient.

To analyze chemical constituent of the amorphous interfacial layer, we obtained HAADF-STEM image and EDS elemental map of the BFO/Si interface. As shown in Fig. 3(a), HAADF-STEM image further confirms the presence of amorphous interfacial layer denoted by the area between the two pink dotted lines. Fig. 3(c) shows EDS elemental map of color mixture of various signals in Fig. 3(b), where Bi-M, O-K and Si-K signals are shown in green, blue and red color, respectively. We observed that interfacial layer denoted by the area between the two white dotted lines mainly contains O-K and Si-K signals. Line profiles in Fig. 3(d) for the BFO/Si interface illustrate that the O-K and Si-K signals are stronger than the Bi-M and Fe-K signals at the amorphous interfacial layer denoted by the pink semitransparent area. Therefore, the interfacial layer are mainly composed of O and Si elements, which would arise from the oxidation of Si surface or the mutual diffusion and reaction between the BFO thin film and Si substrate.

The surface morphology and piezoelectric response of the BFO thin films with different thickness are shown in Fig. 4. The AFM images shown in Fig. 4(a)–(c) were scanned in a square area of $2 \times 2 \mu\text{m}^2$, and the root-mean-square (RMS) roughness were measured to be about 0.89 nm, 0.98 nm, and 3.38 nm for the 110 nm, 270 nm, and 460 nm thin films, respectively. The surface roughness of the BFO thin film apparently increases with increasing thickness, arising from islandlike growth mechanism. The out-of-plane PFM phase images of the BFO thin films are shown in Fig. 4(d)–(f), indicating that the thin films have both up and down polarization domains with a random distribution. Fig. 4(f) shows an electrical written domain pattern for the 460 nm BFO thin film by applied $\pm 18 \text{ V}$ voltage, which confirms the domain orientations and the switchable polarization domains.

The schematic diagram of capacitance configuration for measuring electrical properties is shown in Fig. 5(a). By using metallic mask, Au dots of $100 \mu\text{m}$ in diameter and 50 nm in thickness were evaporated on

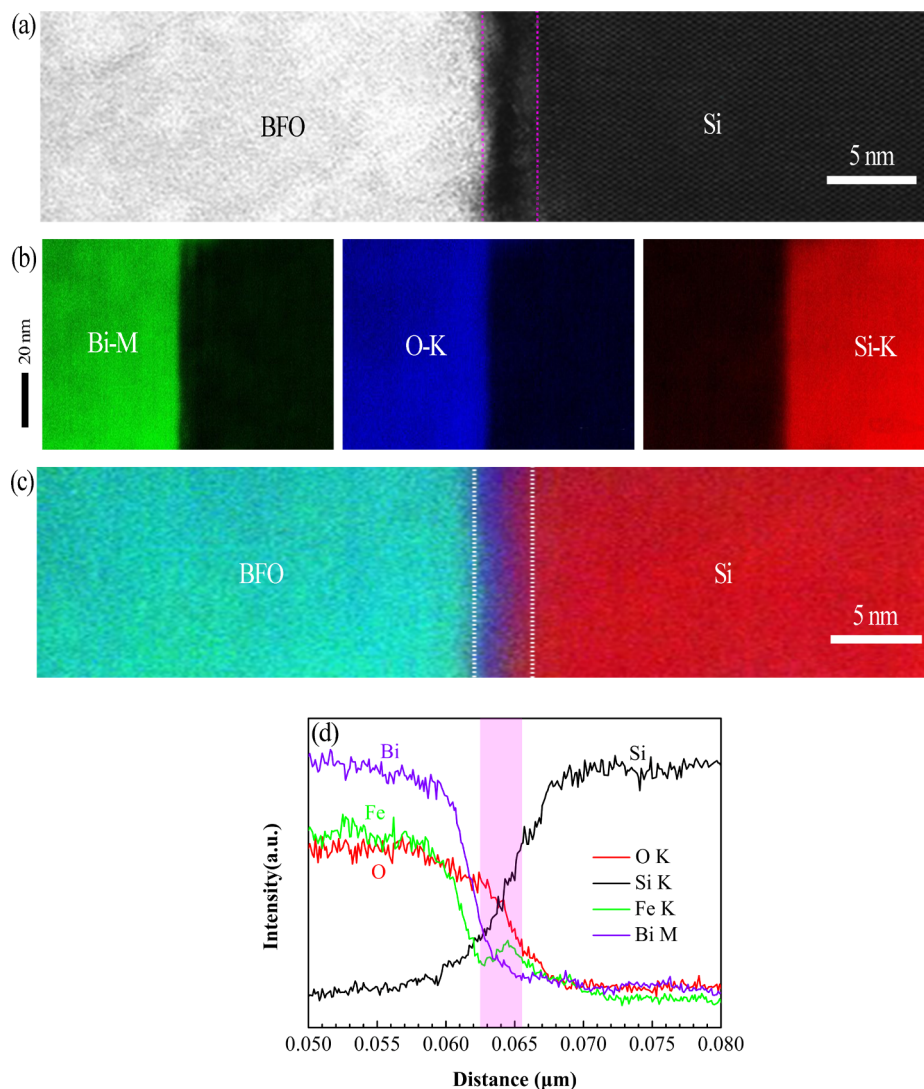


Fig. 3. HAADF-STEM image and EDS elemental map across the BFO/Si interface. (a) HAADF-STEM image of the BFO/Si interface. (b) EDS elemental maps of Bi-M, O-K, and Si-K signals. (c) EDS elemental map of color mixture of various signals. (d) Line profiles for the BFO/Si interface.

the BFO surface to serve as top electrode, and the conducting Si substrate served as bottom electrode. As shown in Fig. 5(b), ferroelectric properties of the BFO thin films with different thickness were demonstrated by the ferroelectric hysteresis loops (P - E loops), which were measured with a frequency of 10 kHz and various applied bias at room temperature. The remnant polarization (P_r) for the 110 nm, 270 nm, and 460 nm BFO thin films are $4.3 \mu\text{C}/\text{cm}^2$, $9.8 \mu\text{C}/\text{cm}^2$, and $20.5 \mu\text{C}/\text{cm}^2$, respectively. By comparison, the obtained remnant polarization is smaller than the epitaxial BFO thin films grown on SrTiO_3 substrates reported by Li *et al.* [23]. The remnant polarization increases with the increase of the film thickness, which should be relevant to the improved crystallinity revealed by the XRD results and may also be a consequence of the reduction of in-plane biaxial tensile strain [24,25]. The measured coercive fields are roughly 1200 kV/cm for the 110 nm film, 800 kV/cm for the 270 nm film, and 650 kV/cm for the 460 nm film, manifesting that the coercive field decreases with the increase of thickness. The change trend of coercive field is in agreement with the results reported by Le Wang *et al.* [26], which can be attributed to the more difficult motion of the domain walls with the decrease of BFO film thickness and therefore larger electric fields are required to carry out the domain reversal [27]. Fig. 5(c) shows the ferroelectric hysteresis loops with applied maximum voltage ranging from 59 V to 99 V for 460 nm BFO thin film, indicating that the BFO film exhibits good ferroelectricity.

Fig. 6(a) shows the current density versus electric field curves measured under dark for the BFO thin films with different thickness. The curves were measured in the sequence of voltage sweeping from $0 \rightarrow -V_{\text{max}} \rightarrow 0 \rightarrow +V_{\text{max}} \rightarrow 0$ at room temperature and plotted in semilogarithmic scales. The 460 nm film has the lowest leakage current, which is in agreement with the consensus that the reduced leakage current, in general, is companied with an improved ferroelectric polarization loop. With decreasing thickness, the 270 nm thin film rather than the 110 nm thin films, however, has a larger leakage current. The discrepancy of the leakage current evolution with the film thickness may arise from a compromise between two factors. One is the worse crystallinity in the thinner films which decreases the film resistivity and another is the existence of the high insulating amorphous interface layer which should play a more important role for the resistivity of the thinner film according to the model of series resistance. Fig. 6(b) shows the current density curves measured under illumination and dark for the 460 nm thin film at room temperature. The current by illumination increases obviously, owing to the increase of the concentration of conductive carriers originated from the transition of the electrons in the valence bands to the conduction bands when photons are absorbed. The curves of current density versus electric field in different thickness with or without laser irradiation apparently emerge linear relationship at low electric field, but begin to occur non-linear features at higher

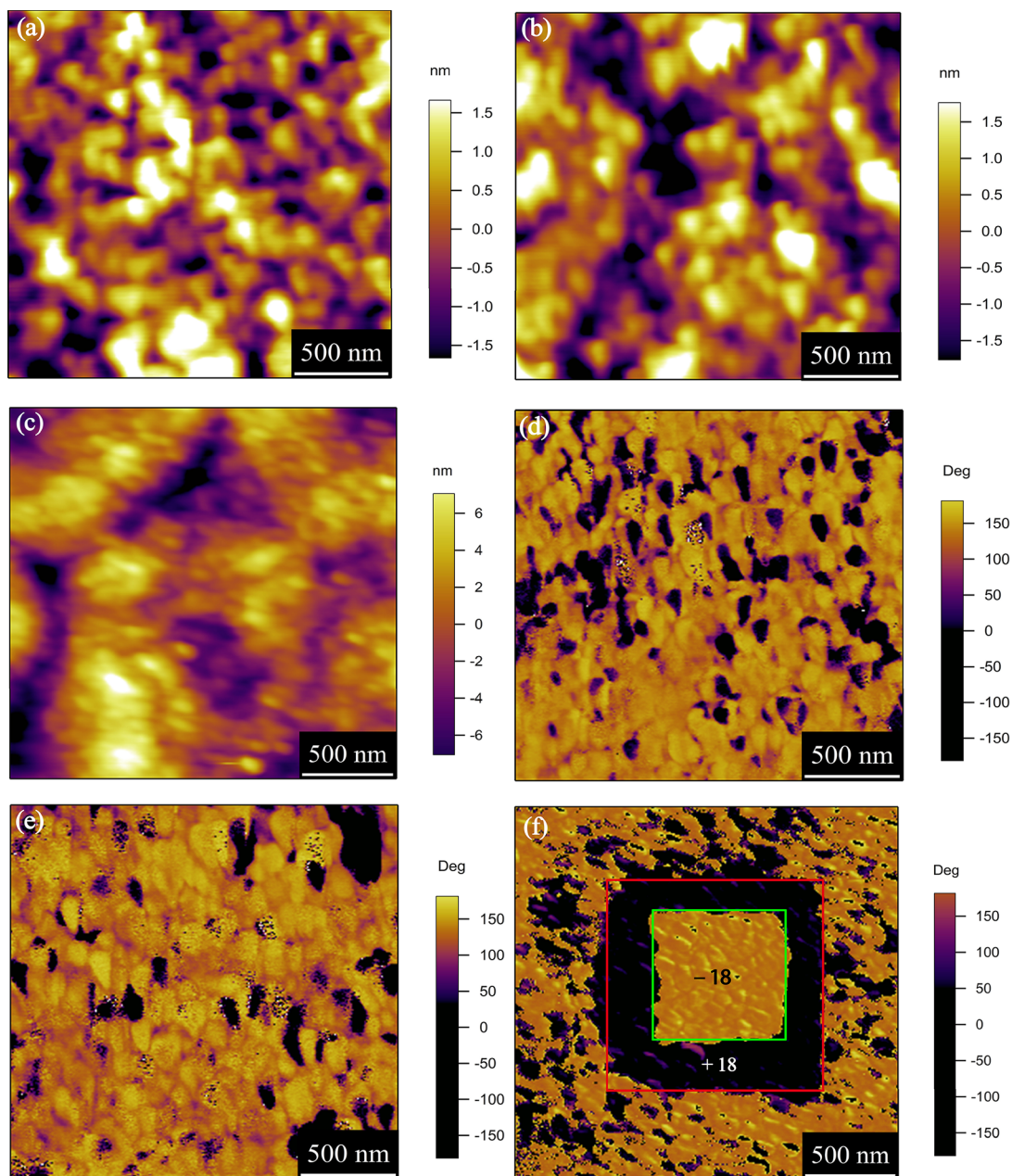


Fig. 4. Surface morphology and PFM phase images of the as-grown BFO thin films. (a)–(c) are the AFM images for the BFO thin films with 110 nm, 270 nm, and 460 nm thickness, respectively. (d)–(f) are the out-of-plane PFM phase images acquired in the same area corresponding in (a)–(c) and in addition, (f) shows an electrical written domain pattern on the 460 nm thin film with ± 18 V voltage.

electric field, because Ohmic conduction plays a leading role at low electric field, whereas non-linear conduction mechanisms, such as space charge limited, Schottky emission or Poole-Frenkel emission, start to become dominant conduction mechanism at higher electric field [28]. Comparing with reported values [29], the observed smaller leakage currents may result from the high insulating amorphous interlayer, which can increase the barrier height due to higher band gap [22].

Moreover, optical properties of the BFO thin films were investigated by spectroscopic ellipsometry which is an optical technique to measure the change of the polarization state of a polarized light beam after reflection from the sample. The ellipsometric parameters ψ and Δ are related to the ratio of the Fresnel reflection coefficients r_p and r_s for polarized light parallel (p) and perpendicular (s) to the incident plane, respectively. This complex reflectance ratio is defined as $\rho = r_p/r_s = \tan(\psi)\exp(i\Delta)$, where $\tan(\psi)$ represents the relative amplitude attenuation

and Δ gives the difference of phase displacement of these two electric field components before and after reflection from the sample. The measured ellipsometric data ψ and Δ for the 270 nm BFO thin films, as shown in Fig. 7(a) and (b), were collected at three angles of incidence (65° , 70° , and 75°) over a spectral range from 1.24 eV to 6.42 eV in ambient condition. The corresponding dielectric function spectra (ϵ_1 , ϵ_2) in Fig. 7(c) were extracted by minimizing the mean square error (MSE) [30] value to fit measured data (ψ , Δ) with a four-medium optical model which consists of Si/interfacial layer/BFO film/surface roughness of the BFO thin film, where the free parameters are surface roughness thickness of BFO thin film, a parameterization of the BFO dielectric function, and the thickness of BFO layer and interfacial layer, respectively. The model parameterization of dielectric function (ϵ_1 , ϵ_2) consists of four Tauc-Lorentz sharing a common Tauc gap and light-frequency lattice dielectric constant (ϵ_∞) [31,32], and the optical properties of the surface roughness layer are modeled by a Bruggeman

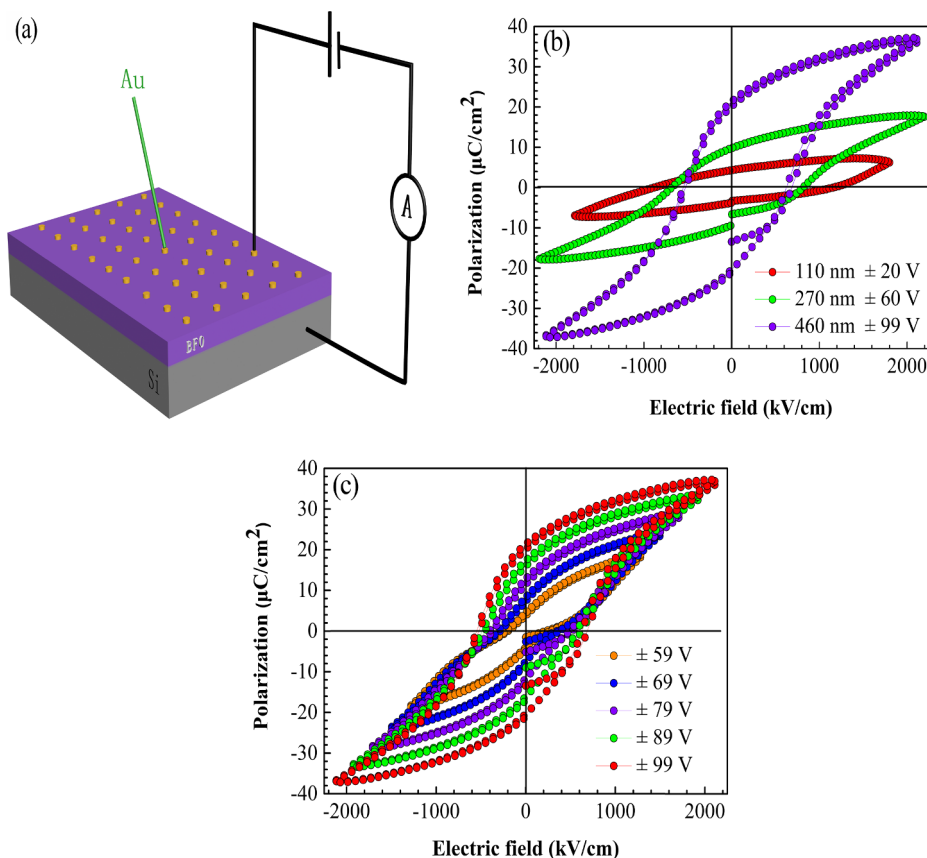


Fig. 5. Ferroelectric hysteresis loops of the BFO thin films measured at 10 kHz. (a) Schematic diagram of capacitance structure. (b) Ferroelectric hysteresis loops for the 110 nm, 270 nm and 460 nm BFO thin films. (c) Ferroelectric hysteresis loops for 460 nm BFO thin film with various voltages (59–99 V).

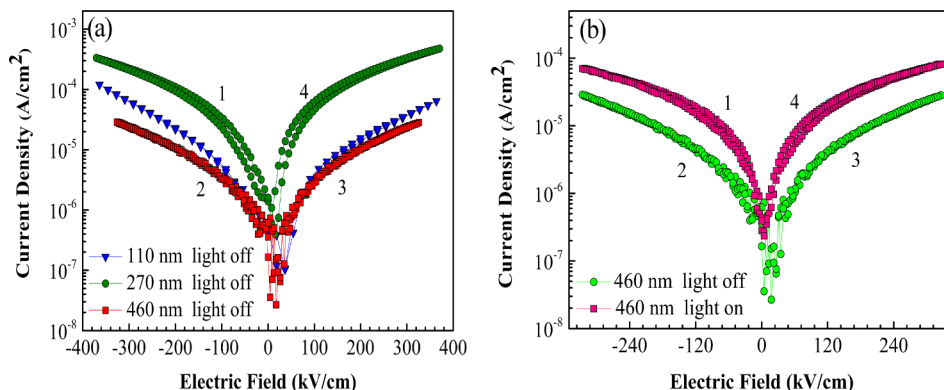


Fig. 6. Current density versus electric field characteristics of the BFO thin films. (a) Current density-electric field curves of the BFO thin films in different thickness without illumination. (b) The dark current and photocurrent density – electric field curves of the 460 nm BFO thin films.

effective medium approximation consisting of a 50% BFO and 50% void mixture [31,33,34]. It is obvious that the fitted ellipsometric spectra sketched in Fig. 7(a) and (b) by black short dash lines fit well with the measured ellipsometric spectra. Fig. 7(d) reveals the obtained relation of refractive index n and extinction coefficient k versus photon energy for the 270 nm BFO thin film, according to $n = \{[\epsilon_1 + (\epsilon_1^2 + \epsilon_2^2)^{1/2}]/2\}^{1/2}$, $k = \{[-\epsilon_1 + (\epsilon_1^2 + \epsilon_2^2)^{1/2}]/2\}^{1/2}$ [33]. The calculated optical absorption coefficient α ($\alpha = 4k\pi/\lambda$) versus photon energy of the BFO thin films with various thicknesses are shown in Fig. 7(e) where k and λ are extinction coefficient and the wavelength of incident light. The results illustrate that as the thickness of thin film increases, the fundamental absorption edge shows a slight red shift trend. Furthermore, we plotted $(\alpha E)^2$ versus photon energy shown in Fig. 7(f) where E is the incident photon energy. We extracted band gap energy of 2.885 eV,

2.837 eV, 2.788 eV for 110 nm, 270 nm, 460 nm BFO thin films corresponding to the absorption edges of 431 nm, 438 nm, 446 nm, respectively. Our measured band gap values are similar to calculated band gap of 2.8 eV for BiFeO₃ by the density-functional based screened exchange method [35]. As shown in the inset, there is a slight but conspicuous increase in band gap energy with decreasing thickness of BFO thin films. By using AFM, the in-plane grain size can be estimated to be about 83 nm, 102 nm, 124 nm for the 110 nm, 270 nm, 460 nm BFO thin films, respectively. Thus, the thicker film with relatively large grain size exhibits smaller band gap, which can be related to the quantum confinement effect [36]. In addition, the change of optical band gap may also be relevant to strain arising from lattice mismatch between BFO thin film and Si substrate. Because of the occurrence of strain relaxation with the increase of thickness, the decreased strain

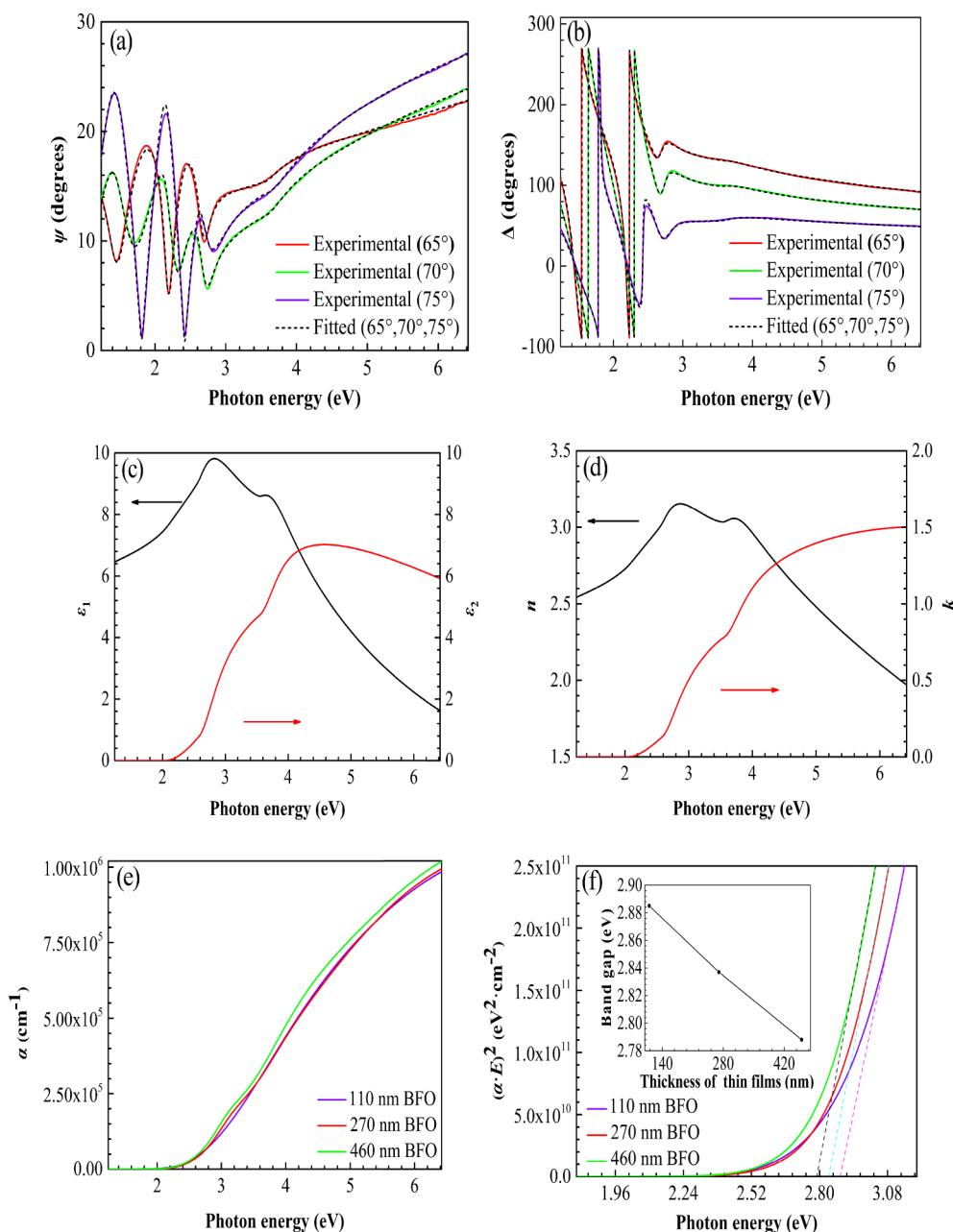


Fig. 7. Optical properties of BFO thin films on Si substrates. (a) and (b) are the measured and fitted spectra of ellipsometric parameter (ψ , Δ) for 270 nm thin film collected at different angles of incidence at room temperature. (c) Photon energy dependence of the real (ϵ_1) and imaginary (ϵ_2) parts of dielectric function of 270 nm BFO thin film. (d) Photon energy dependence of refractive index n and the extinction coefficient k of 270 nm BFO thin film. (e) Photon energy dependence of absorption coefficient of BFO thin film with diverse thicknesses. (f) The band gap energy E_g of BFO thin films with diverse thicknesses are the linear extrapolation from the plotting of $(\alpha E)^2$ versus photon energy by colorful dash lines to $(\alpha E)^2 = 0$, and the inset shows thickness of thin films dependence of band gap. (For interpretation of the references to colour in this figure legend, the reader is referred to the web version of this article.)

may induce the decrease of optical band gap [37,38]. Our data confirm that there is no the presence of an indirect band gap possessed of two distinct slopes in $(\alpha E)^{1/2}$ versus the photon energy characteristic curve.

4. Conclusions

In summary, single-phase BFO thin films have been grown directly on Si (1 0 0) substrate, and the thin films show good ferroelectricity and low leakage current. We found that a predeposition process performed at room temperature and high vacuum conditions is effective and necessary for obtaining the pure-phase BiFeO₃ thin films. By investigating the optical properties of the BFO thin films, it was found that with increasing thickness, the BFO thin films show a red shift in absorption edge, and a decrease in optical band gap. This work sheds light on the potential application of BFO thin films for the design of novel photoelectric devices for information storage and sensing.

Declaration of Competing Interest

The authors declare no competing financial interests.

Acknowledgements

The research was financially supported by the National Basic Research Program of China (Grants Nos. 2017YFA0303604), the National Natural Science Foundation of China (Grants Nos. 11874412, 11674385, and 11721404), and the Youth Innovation Promotion Association of CAS (No. 2018008).

References

- [1] Yoshinori Tokura, Harold Y. Hwang, Nat. Mater. 7 (2008) 694.
- [2] K. Cai, M. Yang, H. Ju, S. Wang, Y. Ji, B. Li, K.W. Edmonds, Y. Sheng, B. Zhang, N. Zhang, S. Liu, H. Zheng, K. Wang, Nat. Mater. 16 (2017) 712.
- [3] J. Seidel, L.W. Martin, Q. He, Q. Zhan, Y.-H. Chu, A. Rother, M.E. Hawkrigde, P. Maksymovych, P. Yu, M. Gajek, N. Balke, S.V. Kalinin, S. Gemming, F. Wang,

- G. Catalan, J.F. Scott, N.A. Spaldin, J. Orenstein, R. Ramesh, *Nat. Mater.* 8 (2009) 229.
- [4] J.W. Reiner, A.M. Kolpak, Y. Segal, K.F. Garrity, S. Ismail-Beigi, C.H. Ahn, F.J. Walker, *Adv. Mater.* 22 (2010) 2919.
- [5] Y.-H. Chu, L.W. Martin, M.B. Holcomb, M. Gajek, S.-J. Han, Q. He, N. Balke, C.-H. Yang, D. Lee, H. Wei, Q. Zhan, P.-L. Yang, A. Fraile-Rodríguez, A. Scholl, S.X. Wang, R. Ramesh, *Nat. Mater.* 7 (2008) 478.
- [6] D. Lebeugle, D. Colson, A. Forget, M. Viret, A.M. Bataille, A. Gukasov, *Phys. Rev. Lett.* 100 (2008) 227602.
- [7] Y. Wang, C. Nelson, A. Melville, B. Winchester, S. Shang, Z.-K. Liu, D.G. Schlom, X. Pan, L.-Q. Chen, *Phys. Rev. Lett.* 110 (2013) 267601.
- [8] S.K. Lee, B.H. Choi, D. Hesse, *Appl. Phys. Lett.* 102 (2013) 242906.
- [9] Y.W. Li, J.L. Sun, J. Chen, X.J. Meng, J.H. Chu, *J. Cryst. Growth* 285 (2005) 595.
- [10] J.T. Heron, J.L. Bosse, Q. He, Y. Gao, M. Trassin, L. Ye, J.D. Clarkson, C. Wang, J. Liu, S. Salahuddin, D.C. Ralph, D.G. Schlom, J. Íñiguez, B.D. Huey, R. Ramesh, *Nature* 516 (2014) 370.
- [11] Q. He, C.-H. Yeh, J.-C. Yang, G. Singh-Bhalla, C.-W. Liang, P.-W. Chiu, G. Catalan, L.W. Martin, Y.-H. Chu, J.F. Scott, R. Ramesh, *Phys. Rev. Lett.* 108 (2012) 067203.
- [12] P. Rovillain, R. de Sousa, Y. Gallais, A. Sacuto, M.A. Méasson, D. Colson, A. Forget, M. Bibes, A. Barthélémy, M. Cazayous, *Nat. Mater.* 9 (2010) 975.
- [13] D. Sando, A. Agbelele, D. Rahmedov, J. Liu, P. Rovillain, C. Toulouse, I.C. Infante, A.P. Pyatakov, S. Fusill, E. Jacquet, C. Carrétéro, C. Deranlot, S. Lisenkov, D. Wang, J.-M. Le Breton, M. Cazayous, A. Sacuto, J. Juraszek, A.K. Zvezdin, L. Bellaiche, B. Dkhil, A. Barthélémy, M. Bibes, *Nat. Mater.* 12 (2013) 641.
- [14] A.Q. Jiang, C. Wang, K.J. Jin, X.B. Liu, J.F. Scott, C.S. Hwang, T.A. Tang, H.B. Lu, G.Z. Yang, *Adv. Mater.* 23 (2011) 1277.
- [15] S.M. Wu, S.A. Cybart, P. Yu, M.D. Rossell, J.X. Zhang, R. Ramesh, R.C. Dynes, *Nat. Mater.* 9 (2010) 756.
- [16] J. Wang, H. Zheng, Z. Ma, S. Prasertchoung, M. Wuttig, R. Droopad, J. Yu, K. Eisenbeiser, R. Ramesh, *Appl. Phys. Lett.* 85 (2004) 2574.
- [17] D. Chen, C.T. Nelson, X. Zhu, C.R. Serrao, J.D. Clarkson, Z. Wang, Y. Gao, S.-L. Hsu, L.R. Dedon, Z. Chen, D. Yi, H.-J. Liu, D. Zeng, Y.-H. Chu, J. Liu, D.G. Schlom, R. Ramesh, *Nano Lett.* 17 (2017) 5823.
- [18] L.W. Martin, Y.-H. Chu, Q. Zhan, R. Ramesh, S.-J. Han, S.X. Wang, M. Warusawithana, D.G. Schlom, *Appl. Phys. Lett.* 91 (2007) 172513.
- [19] J. Zhu, Z. Yin, F. Zhen, Y. Zhao, X. Zhang, X. Liu, J. You, X. Li, J. Meng, H. Liu, W. Jinliang, *J. Cryst. Growth* 459 (2017) 178.
- [20] P. Kharel, S. Talebi, B. Ramachandran, A. Dixit, V.M. Naik, M.B. Sahana, C. Sudakar, R. Naik, M.S.R. Rao, G. Lawes, *J. Phys.: Condens. Matter* 21 (2009) 036001.
- [21] K. Ravaliya, A. Ravalia, D.D. Pandya, P.S. Solanki, N.A. Shah, *Thin Solid Films* 645 (2018) 436.
- [22] D. Hunter, K. Lord, T.M. Williams, K. Zhang, A.K. Pradhan, D.R. Sahu, J.-L. Huang, *Appl. Phys. Lett.* 89 (2006) 092102.
- [23] J. Li, J. Wang, M. Wuttig, R. Ramesh, N. Wang, B. Ruetter, A.P. Pyatakov, A.K. Zvezdin, D. Viehland, *Appl. Phys. Lett.* 84 (2004) 5261.
- [24] H.W. Jang, S.H. Baek, D. Ortiz, C.M. Folkman, R.R. Das, Y.H. Chu, P. Shafer, J.X. Zhang, S. Choudhury, V. Vaithyanathan, Y.B. Chen, D.A. Felker, M.D. Biegalski, M.S. Rzchowski, X.Q. Pan, D.G. Schlom, L.Q. Chen, R. Ramesh, C.B. Eom, *Phys. Rev. Lett.* 101 (2008) 107602.
- [25] M.D. Biegalski, D.H. Kim, S. Choudhury, L.Q. Chen, H.M. Christen, K. Dörr, *Appl. Phys. Lett.* 98 (2011) 142902.
- [26] L. Wang, Z. Wang, K. Jin, J. Li, H. Yang, C. Wang, R. Zhao, H. Lu, H. Guo, G. Yang, *Appl. Phys. Lett.* 102 (2013) 242902.
- [27] J. Pérez de la Cruz, E. Joanni, P.M. Vilarinho, A.L. Kholkin, *J. Appl. Phys.* 108 (2010) 114106.
- [28] C. Wang, M. Takahashi, H. Fujino, X. Zhao, E. Kume, T. Horiuchi, S. Sakai, *J. Appl. Phys.* 99 (2006) 054104.
- [29] K.Y. Yun, D. Ricinchi, T. Kanashima, M. Okuyama, *Appl. Phys. Lett.* 89 (2006) 192902.
- [30] H. Shahrokhbadi, A. Bananej, M. Vaezzadeh, *J. Appl. Spectrosc.* 84 (2017) 915.
- [31] J.F. Ihlefeld, N.J. Podraza, Z.K. Liu, R.C. Rai, X. Xu, T. Heeg, Y.B. Chen, J. Li, R.W. Collins, J.L. Musfeldt, X.Q. Pan, J. Schubert, R. Ramesh, D.G. Schlom, *Appl. Phys. Lett.* 92 (2008) 142908.
- [32] Y. Shen, P. Zhou, Q.Q. Sun, L. Wan, J. Li, L.Y. Chen, D.W. Zhang, X.B. Wang, *Appl. Phys. Lett.* 99 (2011) 141911.
- [33] X. Ji-Ping, R.-J. Zhang, Z.-H. Chen, Z.-Y. Wang, F. Zhang, X. Yu, A.-Q. Jiang, Y.-X. Zheng, S.-Y. Wang, L.-Y. Chen, *Nanoscale Res. Lett.* 9 (2014) 188.
- [34] H. Fujiwara, J. Koh, P.I. Rovira, R.W. Collins, *Phys. Rev. B* 61 (2000) 10832.
- [35] S.J. Clark, J. Robertson, *Appl. Phys. Lett.* 90 (2007) 132903.
- [36] C.V. Ramana, R.S. Vemuri, I. Fernandez, A.L. Campbell, *Appl. Phys. Lett.* 95 (2009) 231905.
- [37] D. Sando, Y. Yang, E. Bousquet, C. Carrétéro, V. Garcia, S. Fusil, D. Dolfi, A. Barthélémy, P. Ghosez, L. Bellaiche, M. Bibes, *Nat. Commun.* 7 (2016) 10718.
- [38] C. Himcinschi, I. Vrejoiu, M. Friedrich, E. Nikulina, L. Ding, C. Cobet, N. Esser, M. Alexe, D. Rafaja, D.R.T. Zahn, *J. Appl. Phys.* 107 (2010) 123524.